FOREX Publication
Open Access | Rapid and quality publishing

International Journal of
Electrical and Electronics Research (IJEER)
Research Article | Volume 14, Issue 3 | Pages 759-770| e-ISSN: 2347-470X

# Computational Investigation of Interface Defects, Doping, and Emitter Thickness Effects in Front-and-Rear Illuminated Bifacial Heterojunction Solar Cells Using COMSOL Multiphysics

**Wafa Bakhat[1*], Asma Benchiheb[2,3], Hamza Lidjici[4], and Fatima Zahra Bakhat[5]**

[1]*LMAVER Laboratory for Renewable Energy Applications and Valorization, University of Laghouat, Algeria, and the Laboratory of Applied Sciences and Didactics, Higher Normal School of Laghouat, Algeria; Email: w.bakhat@lagh-univ.dz*
[2]*Department of Pharmacy, Faculty of Medicine, University of Salah Boubnider Constantine 3, 25000 Constantine, Algeria; Email: asmabenchiheb@yahoo.fr*
[3]*Microsystems and Instrumentation Laboratory, Department of Electronics, Faculty of Technology, University of Frères Mentouri Constantine 1, 25000 Constantine, Algeria; Email: asmabenchiheb@yahoo.fr*
[4]*LMAVER Laboratory for Renewable Energy Applications and Valorization, University of Laghouat, Algeria; Email: ha.lidjici@lagh-univ.dz*
[5]*Process Engineering Laboratory (LGP), University of Laghouat, Algeria; Email: f.bekhat.gpr@lagh-univ.dz*

*Correspondence: *w.bakhat@lagh-univ.dz*

**ABSTRACT-** Bifacial silicon heterojunction (HJ) solar cells have attracted considerable attention due to their high efficiency and capability to utilize illumination from both front and rear sides. In this work, a bifacial HJ solar cell with the structure IMAI/n-a-Si:H/c-Si/p-a-Si:H/ITO is numerically investigated using COMSOL Multiphysics. The device performance is analyzed under front-side, rear-side, and simultaneous bifacial illumination by considering the effects of interface-trap density, donor concentration, and emitter thickness of the n-type amorphous silicon layer. An asymmetric interface-trap configuration is adopted, with$10^{10}(cm^{-2})$at the n-a-Si:H/c-Si interface and $10^{9}(cm^{-2})$ at the c-Si/p-a-Si:H interface. Based on the investigated parameter ranges, a donor concentration of $5.10^{20}(cm^{-3})$ is selected as the reference value, while an emitter thickness of 5 nm provides the best photovoltaic performance within the investigated thickness range. Under the selected parameter set, the simulated device exhibits conversion efficiencies of 26.6%, 20.09%, and 27% under front-side, rear-side, and simultaneous bifacial illumination, respectively. The rear-to-front efficiency ratio is 75.5%, indicating a pronounced front–rear asymmetry. The results indicate that the front-side photovoltaic response remains higher than the rear-side response, which is consistent with the asymmetric interface conditions and the resulting non-uniform recombination and carrier-transport behavior across the device structure. Overall, the findings highlight the importance of interface engineering and appropriate selection of emitter properties in controlling the photovoltaic performance of bifacial heterojunction solar cells.

**Keywords:** Bifacial HJ Solar Cell, Heterojunction, Interface-Trap Density, Ratio for Front and Rear Asymmetry, COMSOL Multiphysics.

**ARTICLE INFORMATION**

**Author(s)**: Wafa Bakhat, Asma Benchiheb, and Hamza Lidjici, Fatima Zahra Bakhat;

**Received**: 28/06/26; **Accepted**: 16/09/26; **Published**: 30/09/26;
**E- ISSN**: 2347-470X;
**Paper Id**: IJEER 2806B12;
**Citation**: 10.37391/ijeer.140310
**Webpage-link**:
https://ijeer.forexjournal.co.in/archive/volume-14/ijeer-140310.html

**Publisher's Note:** FOREX Publication stays neutral with regard to jurisdictional claims in Published maps and institutional affiliations.

## 1. INTRODUCTION

Driven by the accelerating global energy crisis and the pressing need for sustainable alternatives, solar energy has become one of the most compelling renewable resources, offering a clean, virtually inexhaustible, and environmentally responsible solution for future energy production. This growing interest has led to the development of various solar cell technologies aimed at improving efficiency and reducing production costs. Since Bell Laboratories successfully fabricated the world's first practical silicon p–n junction solar cell, the use of silicon-based solar cells has continued to increase [1]. Devices based on electronic semiconductors, particularly crystalline silicon (c-Si) and thin-film semiconductor materials, are widely used for photovoltaic energy conversion [2-4]. Crystalline silicon solar systems are typically built using two main types of modules: monocrystalline and multicrystalline. Compared to multicrystalline materials, single-crystal semiconductors exhibit superior electrical properties, achieving efficiencies of up to 20%. However, due to the high cost of wafer-based crystalline technology, monocrystalline photovoltaic modules are less cost-effective [5],[6]. Consequently, recent research has focused on developing alternative technologies that can achieve high efficiency while reducing manufacturing costs. Among these promising technologies are heterojunction solar cells (HJSCs), which are formed by combining two

FOREX Publication
Open Access | Rapid and quality publishing
International Journal of Electrical and Electronics Research (IJEER)
Research Article | Volume 14, Issue 3 | Pages 759-770| e-ISSN: 2347-470X

semiconductor materials with different energy band gaps. Heterojunctions were first studied in 1974 by Fuhs [7], and in 1983 the first solar cell based on this structure was fabricated [8],[9]. Bifacial solar cells are of significant interest due to their higher efficiency potential and the increasing demand to enhance photovoltaic power generation. The bifacial architecture, which incorporates metal grid lines on both the front and rear surfaces, enables light absorption from both sides. Under specific operating conditions, this configuration can generate up to 20% more power compared to conventional single-sided solar cells [10-14].

In this work, a bifacial heterojunction solar cell with the structure IMAI / n-a-Si:H / c-Si / p-a-Si:H / ITO is numerically investigated using COMSOL Multiphysics. The device performance is analyzed under front, rear, and bifacial illumination by considering the effects of interface defect density, donor concentration, and emitter thickness. An asymmetric defect configuration is assumed at the front and rear interfaces to reflect realistic non-uniform interface conditions. The simulations indicate that a donor concentration of $\mathbf{5.10^{20}}\boldsymbol{cm^{-3}}$ and an emitter thickness of 5 nm correspond to the optimum conditions considered in this study. Under these conditions, the simulated conversion efficiencies reach 26.60%, 20.09%, and 27% under front-, rear-, and bifacial illumination, respectively. The resulting rear-to-front efficiency ratio is 75.53%, which is close to the experimentally reported value of approximately 77%. This agreement indicates that the simulated front–rear performance asymmetry is consistent with that observed experimentally in bifacial silicon solar cells.

## 2. THE NUMERICAL RESOLUTION EQUATIONS

### 2.1. The equations governing the system under consideration

The modeling and simulation of solar cells in one-dimension (1D) using COMSOL-Multiphysics software are based on the numerical solution of the fundamental drift-diffusion (DDM) equations in semiconductors, implemented through the finite element method [15]. These equations consist of the following: the Poisson equation (1), the continuity equations (2), and the transport equations for electrons and holes (3) [16-17]:

$$div\left(\epsilon \cdot \overrightarrow{grad}\, V\right) = -q \cdot (p - n + dop) \quad (1)$$

$$g_n - r_n = -\frac{1}{q}\vec{\nabla}\overrightarrow{J_n}$$
$$g_p - r_p = \frac{1}{q}\vec{\nabla}\overrightarrow{J_p} \quad (2)$$

$$\overrightarrow{J_n} = qn\mu_n\vec{E} + qD_n\vec{\nabla}n$$

$$\overrightarrow{J_p} = qp\mu_p\vec{E} - qD_p\vec{\nabla}p \quad (3)$$

Where:
$\varepsilon_0$: Absolute dielectric constant.
$\varepsilon_r$ : Relative dielectric constant.
ψ(x): Electrostatic potential at the x position of the solar cell.
q: Electron elemental charge.
n / p: Electron/hole.
$dop = N_D^+ - N_A^- : N_D^+ \; and \; N_A^-$ : denote the ionized donor and acceptor concentrations, respectively.
x: The position in the cell.
$J_{n,p}$ : is the current density of electrons and holes.
$G_{n,p}$: is the rate of electron and hole generation.
$R_{n,p}$ : is the recombination rate of the electron and hole.
$\mu_{n,p}$: mobilities of electron and hole.
E: Electric field.
$D_{n,p}$ : Diffusion constant for electrons, holes.

We assumed ideal Ohmic contacts at the external electrical contacts, and COMSOL Multiphysics® automatically determined the band offsets at the hetero-interfaces from the specified material properties. Table 1 summarizes the material, mobility, and doping parameters used in the simulations, along with their corresponding references.

The semiconductor equations were solved under steady-state conditions using a Stationary nonlinear solver with automatic variable scaling.

$$G(\gamma, x) = \alpha(\gamma) \cdot \emptyset(\gamma) \cdot \left(1 - R(\lambda)\right) \cdot e^{-\alpha(\gamma)\cdot x} \quad (4)$$

In this context, α(γ) represents the absorption coefficient corresponding to wavelength γ. Ø(γ) is the flux of incoming photons per square centimeter per second for each bandwidth unit, and $R(\lambda)$is associated to the fraction of photons that are reflected by the surface. The total photo-generation rate, $G(\gamma, x)$ is obtained by the integration of Eq. (4) across the full spectrum of sunlight wavelengths. The complete multilayer cell structure was included in the optical calculations, the wavelength-dependent optical properties and layer thicknesses were used within the Beer–Lambert absorption model to determine the local photo-generation profile over the wavelength range of [280–1300] nm under the standard AM1.5G solar spectrum. The wavelength-dependent refractive index n and extinction coefficient $k$ of the constituent materials were used to determine their optical absorption properties. The optical constants were obtained from RefractiveIndex.INFO [19], while the AM1.5G solar spectrum was taken from ASTM G173. The optical model accounted for the absorption of the constituent layers. Separate photo-generation expressions were defined for the three illumination conditions considered in this work: front-side illumination$G_{ph,Front}$, rear-side illumination$G_{ph,Rear}$, and bifacial illumination $G_{ph,tot}$. For each illumination condition, the corresponding photo-generation rate was applied to the semiconductor domains in the COMSOL Semiconductor interface. The resulting photo-generation profiles were subsequently coupled to the semiconductor transport equations

FOREX Publication
Open Access | Rapid and quality publishing
International Journal of Electrical and Electronics Research (IJEER)
Research Article | Volume 14, Issue 3 | Pages 759-770| e-ISSN: 2347-470X

to calculate the photovoltaic response under front, rear, and bifacial illumination.

### 2.3. Illumination Conditions and Bifacial Efficiency Definition

For the optical simulations, the standard AM1.5G solar spectrum at 1-sun irradiance, corresponding to an incident power density of $100\,mW/cm^2$, is considered for each illuminated surface. Under front-side illumination, the front surface is exposed to 1-sun AM1.5G irradiation, whereas under rear-side illumination, the rear surface is exposed to 1-sun AM1.5G irradiation. For simultaneous bifacial illumination, both the front and rear surfaces are simultaneously exposed to 1-sun AM1.5G irradiation. Thus, the total incident power density under bifacial illumination is given by:

$$P_{in,total} = P_{in,Front} + P_{in,Rear} = 100 + 100 = 200\,\frac{mW}{cm^2} \quad (5)$$

The conversion efficiency is calculated from the maximum output power according to:

$$E_{ff} = \frac{P_{max}}{P_{in}} \times 100 \quad (6)$$

For simultaneous bifacial illumination, the bifacial conversion efficiency is therefore determined by considering the total incident power from both illuminated surfaces:

$$E_{ff,bifacial} = \frac{P_{max,bifacial}}{P_{in,Front} + P_{in,Rear}} \times 100 \quad (7)$$

Accordingly, when both surfaces are illuminated under 1-sun AM1.5G conditions, the denominator corresponds to a total incident power density of $P_{in,total} = 200\,mW/cm^2$.

### 2.4. Interface Recombination Modeling

Interface recombination was modeled in COMSOL using the Shockley–Read–Hall (SRH) recombination framework for a single discrete interface-trap energy level. The interface-traps were introduced at the n-a-Si:H/c-Si interface, which was treated as a recombination-active boundary rather than as a bulk interface-trap region. The interface-trap parameters were defined as model variables in COMSOL and assigned to the corresponding interface. The interface-trap density $N_{st}$ was varied over the investigated range, while the remaining trap parameters were maintained at their reference values during each parametric study. The trap energy level, carrier-capture cross-sections, and thermal velocities were specified according to the parameter set used in the corresponding simulations. This procedure allows the individual effect of the investigated interface parameter on the photovoltaic performance to be isolated.The SRH formulation accounts for trap-assisted carrier recombination through the discrete interface state [20], [21]. The corresponding equations used to describe the interface recombination are given in *Eq (8-12).*

$$e_n^{(i)} = cN_c^{(i)} \exp\left(\frac{E_t^{(i)} - E_c}{KT}\right) \quad (8)$$

$$e_p^{(i)} = cN_V^{(i)} \exp\left(\frac{E_V^{(i)} - E_t}{KT}\right) \quad (9)$$

$$j_{s,n} = \left(c\, n^{(i)}(1 - f_t) - e_n^{(i)} f_t\right) N_{st} \quad (10)$$

$$j_{s,p} = \left(c\, p^{(i)} f_t - e_p^{(i)}(1 - f_t)\right) N_{st} \quad (11)$$

$$j_{s,n}^{(1)} + j_{s,n}^{(2)} = j_{s,p}^{(1)} + j_{s,p}^{(2)} \quad (12)$$

These relations were implemented at the n-a-Si:H/c-Si hetero-interface in COMSOL Multiphysics using a Weak Contribution applied to the corresponding boundary.

$$e_{const}\left[j_{s,n}^{(1)} test\left(down(N_e)\right) + j_{s,n}^{(2)} test\left(up(N_e)\right) - j_{s,p}^{(1)} test\left(down(P_h)\right) - j_{s,p}^{(2)} test\left(up(P_h)\right)\right] \quad (13)$$

Where $e_n^{(i)}$, $e_p^{(i)}$ is electron and hole emission rate from trap level into the valence band, $N_c^{(i)}$, $N_V^{(i)}$effective density of states corresponding to the conduction and valence bands, $E_t^{(i)}$trap energy level, $E_c$ conduction-band minimum, $E_V^{(i)}$is the effective density of states in the valence band, and c is a constant. (often includes capture cross-section and thermal velocity), $K_B$ boltzman constant, T temperature, $N_{st}$ trap density of the interface surface, $f_t$ Occupation probability of the trap, $n^{(i)}$, $p^{(i)}$ electron and hole concentration, $j_{s,n}^{(1)}$, $j_{s,n}^{(2)}$, $j_{s,p}^{(1)}$, $j_{s,p}^{(2)}$ hole and electron recombination /generation current density.

The superscript (*i*), where *i* = 1, 2, specifies whether the emission rate is evaluated on the left or right side of the boundary, respectively.

## 3. SOLAR CELL DEFINITION

*Figure 1.* illustrates the architecture of the investigated heterojunction (HJ) solar cell (*a*), together with representative physical and electrical outputs obtained from the numerical model, including the band diagram (*b*), carrier concentration distributions (*c*), and current density–voltage (J–V) characteristics (d). The device structure consists of IMAI/n-a-Si:H/c-Si/p-a-Si:H/ITO, where the n-a-Si:H, c-Si, and p-a-Si:H layers serve as the emitter, absorber, and back-surface-field (BSF) layers, respectively. The IMAI layer acts as the front transparent conductive layer and consists of a laser-treated ITO/Mo–Ag/ITO composite layer [22]. In the present numerical model, the IMAI composite is represented as a single effective layer, while the rear ITO layer serves as the rear transparent conductive layer, enabling illumination from both sides of the device. The IMAI and rear ITO layers were explicitly included as conductive material domains in the numerical model. The layer thicknesses used in the simulations were fixed at 80 nm for the front IMAI layer, 10 nm for n-a-Si:H, 230 µm for c-Si, 10 nm for p-a-Si:H, and 200 nm for the rear ITO layer. The optical properties of the constituent layers were included in the optical model through their wavelength-dependent refractive index and extinction

FOREX Publication
Open Access | Rapid and quality publishing
International Journal of Electrical and Electronics Research (IJEER)
Research Article | Volume 14, Issue 3 | Pages 759-770| e-ISSN: 2347-470X

coefficient, and the resulting absorption was used to determine the photogeneration profiles under front, rear, and bifacial illumination.The front electrical contact was set as the voltage reference with $(V = 0V)$, while the rear contact was assigned a terminal voltage $V_0$. The J–V characteristics were obtained by sweeping the rear-terminal voltage from 0 to 0.9 V with a step size of 0.01 V. Both external contacts were modeled as ideal Ohmic contacts. The n-a-Si:H/c-Si and p-a-Si:H/c-Si heterojunctions were modeled using the thermionic-emission formulation available in the Semiconductor Module. The coupled semiconductor equations were solved using a finite-element formulation, with Maxwell–Boltzmann statistics adopted for the carrier-density formulation. A mesh-convergence study was performed to ensure adequate numerical resolution of the thin semiconductor layers and heterointerfaces. As shown in *table 1*, the maximum element size was progressively reduced from 0.461 to 0.15, while the calculated $J_{SC}, V_{OC}, FF$ *and* $E_{ff}$ exhibited only negligible variations, indicating that the solution was mesh-converged within the investigated range. Particular attention was given to the nanometre-scale amorphous layers and the n-a-Si:H/c-Si and c-Si/p-a-Si:H heterointerfaces. Accordingly, the Finer mesh was selected for the subsequent simulations. The electron and hole mobilities were treated as constant material parameters throughout the donor-concentration sweep, and no doping-dependent mobility model was employed. The remaining material, electrical, doping, and device parameters employed in the simulations are summarized in *table 2.*

**Table 1. Mesh Parameters and Refinement Levels Used in the Numerical Simulation**

| Mesh (Finer) Maximum element size | $J_{SC}(mA/cm^2)$ | $V_{OC}(V)$ | $E_{ff}(\%)$ | $FF(\%)$ |
|---|---|---|---|---|
| 0.461 | 44.123 | 0.7209 | 25.921 | 81.5 |
| 0.35 | 44.118 | 0.7211 | 25.928 | 81.5 |
| 0.25 | 44.107 | 0.7214 | 25.941 | 81.53 |
| 0.15 | 44.106 | 0.7216 | 25.945 | 81.52 |

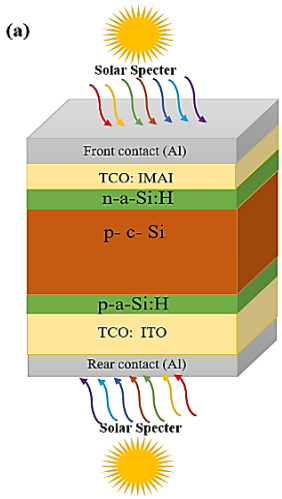


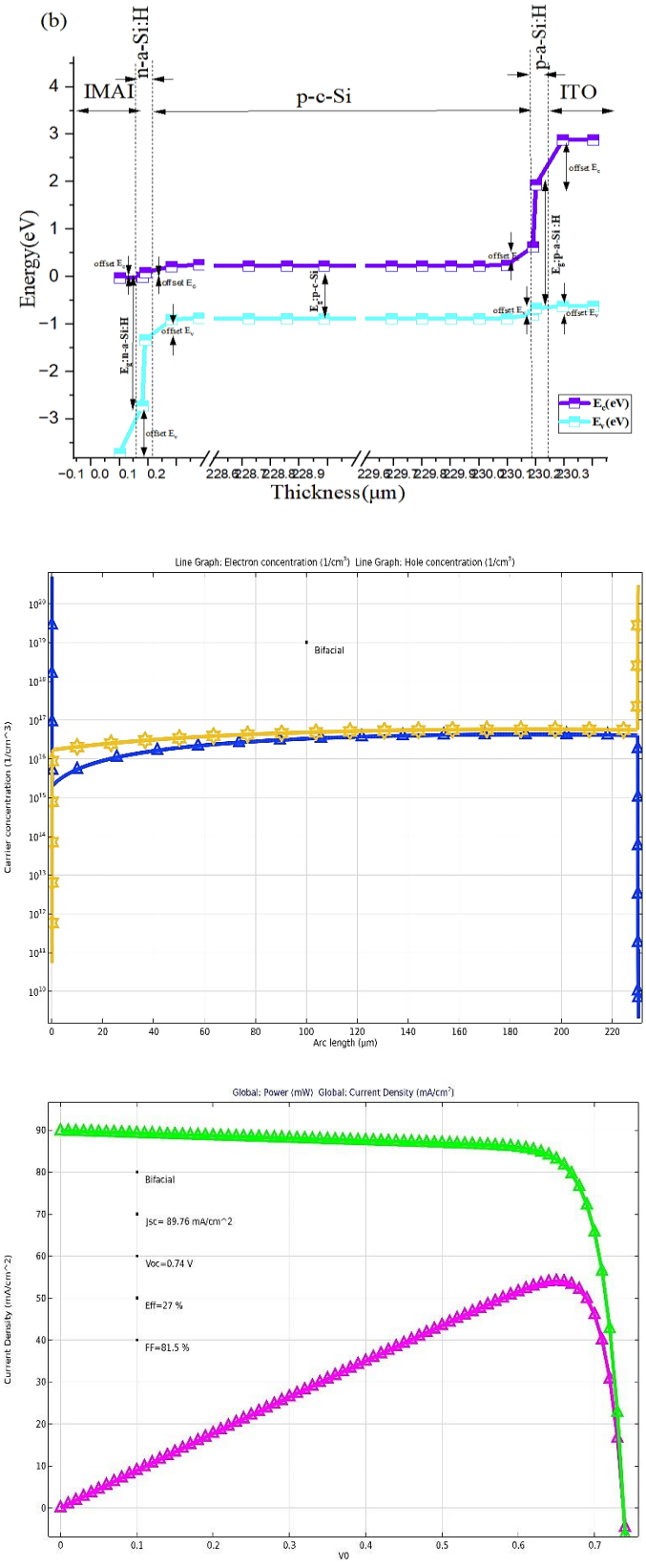


**Figure 1**. Schematic structure of the HJ solar cell (a) and simulated distributions of carrier concentration (b), recombination rate (c), and J–V characteristics (d)

FOREX Publication
Open Access | Rapid and quality publishing
International Journal of Electrical and Electronics Research (IJEER)
Research Article | Volume 14, Issue 3 | Pages 759-770| e-ISSN: 2347-470X

**Table 2. Input Parameters of Various Layers Used in Simulation**

| Input Parameters | ITO [22][23] | IMAI [22] | n-a-Si:H [23][24] | p-a-Si:H [23][24] | c-Si [23][24] |
|---|---|---|---|---|---|
| Layer thickness ($\mu m$) | 0.2 | 0.08 | Value [0.005−0.01] | 0.01 | 230 |
| Relative permittivity $\varepsilon$ | 3.9 | 3.8 | 11.9 | 11.9 | 11.9 |
| Electron affinity $\chi\ (eV)$ | 3.8 | 4.05 | 3.8 | 3.8 | 4.05 |
| Band gap $E_g(eV)$ | 3.8 | 3.7 | 1.74 | 1.7 | 1.12 |
| The conduction-band density of states $N_c(cm^{-3})$ | $2.1 \times 10^{20}$ | $2.2 \times 10^{20}$ | $1 \times 10^{20}$ | $1 \times 10^{20}$ | $2.8 \times 10^{19}$ |
| The density of states in the valance band $N_V(cm^{-3})$ | $2.1 \times 10^{20}$ | $2.2 \times 10^{20}$ | $1 \times 10^{20}$ | $1 \times 10^{20}$ | $1.04 \times 10^{19}$ |
| Electron mobility $\mu_n(cm^2/V.s)$ | 21 | 45 | 10 | 10 | 1040 |
| Electron mobility $\mu_h(cm^2/V.s)$ | 10 | 10 | 1 | 1 | 412.9 |
| Doping concentration of donors $N_d(cm^{-3})$ | 0 | $5 \times 10^{18}$ | Value $[1 \times 10^{19} - 1 \times 10^{21}]$ | 0 | 0 |
| Acceptor doping concentration $N_a(cm^{-3})$ | $1 \times 10^{20}$ | 0 | 0 | $9 \times 10^{21}$ | $1.5 \times 10^{16}$ |
| Layer density $\rho\ (c/cm^3)$ | 7.14 | 10.10 | 2.328 | 2.328 | 2.328 |

The interface-trap parameters used in the numerical model are listed in *table 3*. In the present device, $N_{st}$ is systematically varied at the n-a-Si:H/c-Si heterointerface from $10^9 cm^{-2}$ to $10^{17} cm^{-2}$ to investigate the influence of interface-state density over a broad range, covering different interface conditions. This range was selected based on the wide variation of interface-state densities considered in numerical studies of silicon heterojunction solar cells [23],[25]. The parameters of the other interfaces remain constant throughout the simulations. The traps are represented by a single discrete energy level rather than a continuous energy distribution; therefore, $N_{st}$ is expressed in $cm^{-2}$.The bulk trap-assisted recombination was modeled using the Shockley–Read–Hall (SRH) formulation, with the trap energy level assumed to be approximately at midgap. The parameters $E_t$, $\sigma_n$, $\sigma_p$, and $v_{th}$ denote the trap energy, electron and hole capture cross-sections, and carrier thermal velocity, respectively.

At the n-a-Si:H/c-Si interface, interface recombination was also modeled using the SRH formalism with a single discrete interface-trap level. The interface-trap energy was defined as ($E_t$=$E_v + \Delta E_t$), with ($\Delta E_t$=0.1 eV). The corresponding interface-trap density, carrier capture cross-sections, and thermal velocity are given in *table 3*.

**Table 3. Interface-trap parameters used in the numerical model**

| Input Parameters | Value |
|---|---|
| Surface-state density$N_{st}(cm^{-2})$ | $[10^9 - 10^{17}]$[25] |
| Defect energy level $E_t(eV)$ | $E_v + \Delta E_t$ |
| Energy-level offset $\Delta E_t(eV)$ | 0.1 |
| Electron capture cross-section $\sigma_n$ | $10^{-16}$[26] |
| Hole capture cross-section $\sigma_p$ | $10^{-16}$[26] |
| Thermal velocity $v_{th}(cm.s^{-1})$ | $10^7$[23] |

# 4. RESULTS AND DISCUSSION

## 4.1 Effect of n-a-Si:H/c-Si Interface-trap Density on HJ Silicon Solar Cells under Front and Rear Illumination

This improvement in solar cell performance with decreasing interface-trap density $N_{st}$ is associated with improved electronic properties of the n-a-Si:H/c-Si interface. Lower defect densities reduce trap-assisted recombination (Shockley–Read–Hall) and help preserve favorable band bending and energy band alignment, thereby facilitating the transport and collection of photo-generated carriers [25]. In this work, the interface-trap density $N_{st}$ at the n-a-Si:H/c-Si front interface is systematically varied under asymmetric front–rear illumination conditions to evaluate its impact on device performance over the investigated range $10^9$ *to* $10^{17}$ $cm^{-2}$.

FOREX Publication
Open Access | Rapid and quality publishing
International Journal of Electrical and Electronics Research (IJEER)
Research Article | Volume 14, Issue 3 | Pages 759-770| e-ISSN: 2347-470X

To isolate the effect of front-interface recombination, an asymmetric configuration is adopted in which the rear c-Si/p-a-Si:H interface is kept constant at $N_{st} = 10^{9} cm^{-2}$, while the front interface-trap density is varied. The front interface-trap density is initially set to $N_{st} = 10^{10} cm^{-2}$ , for the baseline configuration [23],[25]. The investigated $N_{st}$ range extends to high trap densities to characterize the device response under progressively severe interface trapping and to evaluate its limiting sensitivity and asymptotic behavior. The upper values should therefore not be interpreted as representative experimentally achievable interface-state densities. The simulations were carried out under standard operating conditions, where the temperature was fixed at 300 K, and the standard AM1.5G solar spectrum was used as the illumination source.

The results, as shown in *Figure 2.(a)–(d)*, indicate that Specifically, decreases $J_{SC}^{Front}$, $J_{SC}^{Rear}$ , $J_{SC}^{Bifacial}$ slightly with increasing $N_{st}$, whereas the decrease in $V_{OC}^{Front}$, $V_{OC}^{Rear}$ , $V_{OC}^{Bifacial}$ becomes more pronounced, indicating that recombination-induced voltage degradation is the dominant loss mechanism , and efficiency $E_{ff}^{Front}$, $E_{ff}^{Rear}$ , $E_{ff}^{Bifacial}$ the degradation decreases gradually. However, beyond $N_{st} < 10^{13} cm^{-2}$ , they progressively approach a saturation regime, indicating that the device enters a recombination-limited region where further increases in interface-trap density have a marginal effect on performance. In addition, the fill factor $FF^{Front}$,$FF^{Rear}$, $FF^{Bifacial}$exhibits increasing interface-trap density $N_{st}$ may therefore increase transport and recombination losses and contribute to an increase in the effective series resistance effects at high interface-trap density levels.

The obtained trend is qualitatively consistent with previous numerical results [23],[25],[26], where the short-circuit current remains nearly unchanged at low interface-trap densities and begins to decrease when the interface-trap density reaches the order of $10^{12}\ cm^{-2}$. This behavior is generally attributed to the increasing contribution of interface-related recombination as the interface-trap density becomes sufficiently high. Although the device structures and material systems considered in the two studies are different, the similar trend supports the physical interpretation of the influence of interface-trap density on carrier recombination and photovoltaic performance.

Interestingly, the bifacial ratio : $\text{Ratio}(E_{ff}) = \frac{E_{ff}^{Rear}}{E_{ff}^{Front}}$ exhibits an increasing trend from 74.23% to 77.32% as $\uparrow N_{st}$ increases, this behavior is explained by the stronger degradation of front-side performance compared to rear-side response, which enhances the apparent front–rear asymmetry of the device under high recombination conditions. This is evident in the results in Table 4, where we observe that the difference, $\uparrow \Delta J_{SC} = J_{SC}^{Front} - J_{SC}^{Rear}$ , $\uparrow \Delta V_{OC} = V_{OC}^{Front} - V_{OC}^{Rear}$ , $\uparrow \Delta E_{ff} = E_{ff}^{Front} - E_{ff}^{Rear}$ , $\uparrow \Delta FF = FF^{Front} - FF^{Rear}$ with $\downarrow N_{st}$ decreasing , Overall the results demonstrate that low interface-trap densities $\approx 10^{10}\ cm^{-2}$ are essential to achieve optimal photovoltaic performance, while higher interface-trap densities significantly deteriorate device efficiency. These findings highlight the critical role of interface engineering in minimizing recombination losses and optimizing bifacial heterojunction solar cell performance.

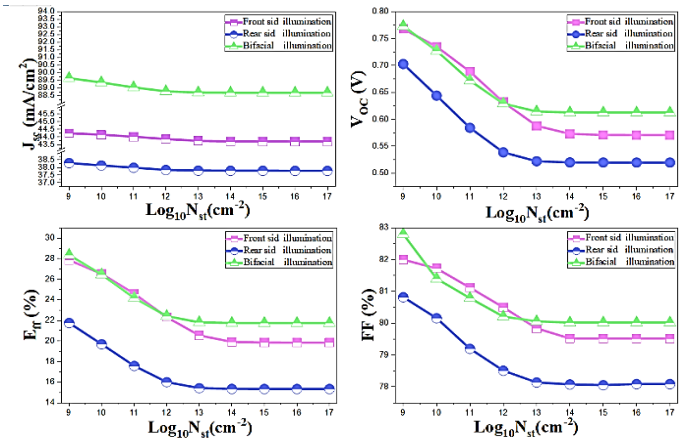


**Figure 2**. Variation of $J_{SC}$, $V_{OC}$, $FF$, and $E_{ff}$ with n-a-Si:H/c-Si Interface-Trap Density under Front and Rear Illumination

**Table.4 Front–Rear Performance Differences ($\Delta J_{SC}$, $\Delta V_{OC}$, $\Delta E_{ff}$, $\Delta FF$) and Front–to-Rear Ratio at Selected Interface-Trap Densities**

| *Interface-Trap Density*($cm^{-2}$) | $\Delta J_{SC}$($mA/cm^2$) | $V_{OC}$(V) | $\Delta E_{ff}$ (%) | $\Delta FF$(%) | $Rear - to - front\ Ratio$ (%) |
|---|---|---|---|---|---|
| $10^{10}$ | 6.012 | 0.091 | 6.834 | 1.56 | 74.23 |
| $10^{13}$ | 5.942 | 0.0659 | 5.117 | 1.7 | 75.09 |
| $10^{16}$ | 5.91 | 0.0511 | 4.501 | 1.43 | 77.32 |

## 4.2. Effect of n-a-Si:H Layer Doping Concentration on HJ Silicon Solar Cells under Front and Rear Illumination

The variation in solar-cell performance with donor concentration may be associated with changes in the electrical properties of the n-a-Si:H emitter layer. Increasing the donor concentration can modify the electrostatic properties of the heterojunction and facilitate carrier transport and collection, which may influence the recombination losses and the resulting photovoltaic performance.

In this work, the donor concentration $N_d$ of the n-a-Si:H layer was systematically varied under asymmetric front- and rear-side illumination conditions to evaluate its effect on the device performance over the investigated range $1.10^{19} to\ 5.10^{20} cm^{-3}$ ,To isolate the effect of emitter doping, all other structural and material parameters were kept constant throughout the simulations. In addition, a fixed interface-trap density of $N_{st} = 10^{10}\ cm^{-2}$ was assumed at the front interface, while the rear interface-trap density was set to $N_{st} = 10^{9}\ cm^{-2}$.

The simulations were carried out under standard operating conditions, with the temperature fixed at 300 K and the standard AM1.5G solar spectrum used as the illumination source.

FOREX Publication
Open Access | Rapid and quality publishing
International Journal of Electrical and Electronics Research (IJEER)
Research Article | Volume 14, Issue 3 | Pages 759-770| e-ISSN: 2347-470X

The results, presented in *Figure 3. (a)–(d),* $J_{SC}^{Front}$, $J_{SC}^{Rear}$, $J_{SC}^{Bifacial}$ and $V_{OC}^{Front}$, $V_{OC}^{Rear}$, $V_{OC}^{Bifacial}$ and $E_{ff}^{Front}$, $E_{ff}^{Rear}$, $E_{ff}^{Bifacial}$ show that the photovoltaic parameters vary slightly with increasing donor concentration $N_d$. This behavior is attributed to the enhanced electronic transport properties of the n-a-Si:H layer and the reduced impact of Shockley–Read–Hall (SRH) recombination at the hetero-interfaces, leading to improved carrier collection and photovoltaic performance.

The slight decrease in $FF^{Front}$,$FF^{Rear}$, $FF^{Bifacial}$, may reflect a limited increase in transport- and recombination-related losses at higher doping concentrations. Nevertheless, the overall improvement in the photovoltaic parameters indicates that the beneficial effects of increased donor concentration generally outweigh these losses. This behavior is consistent with previous findings reported in the literature [23],[27],[28]. Interestingly, the rear-to-front efficiency ratio: $\text{Ratio}(\text{E}_{ff}) = \frac{\text{E}_{ff}^{Rear}}{\text{E}_{ff}^{Front}}$ exhibits an increasing trend from 74.23% to 75.1 % as $\uparrow N_d$ (as the donor concentration increases), reflecting a slight reduction in the relative difference between the front- and rear-side efficiencies. This behavior is also evident in the results presented in *table 5*, where the differences between the front- and rear-side photovoltaic parameters decrease with increasing donor concentration.$\uparrow \Delta J_{SC} = J_{SC}^{Front} - J_{SC}^{Rear}$, $\uparrow \Delta V_{OC} = V_{OC}^{Front} - V_{OC}^{Rear}$, $\uparrow \Delta E_{ff} = E_{ff}^{Front} - E_{ff}^{Rear}$, $\uparrow \Delta FF = FF^{Front} - FF^{Rear}$ with $\uparrow N_d$ (increases), Overall, the results indicate that increasing the donor concentration in the n-a-Si:H emitter layer generally improves the photovoltaic performance of the bifacial heterojunction solar cell over the investigated concentration range, particularly in terms of the photovoltaic parameters.

These findings highlight the important role of donor concentration in influencing carrier transport and the balance between recombination and transport processes, thereby affecting the photovoltaic performance of bifacial heterojunction solar cells. Based on the overall photovoltaic response obtained over the investigated concentration range$\approx 5.10^{20}\ cm^{-3}$ was selected as the reference donor concentration for the subsequent simulations.

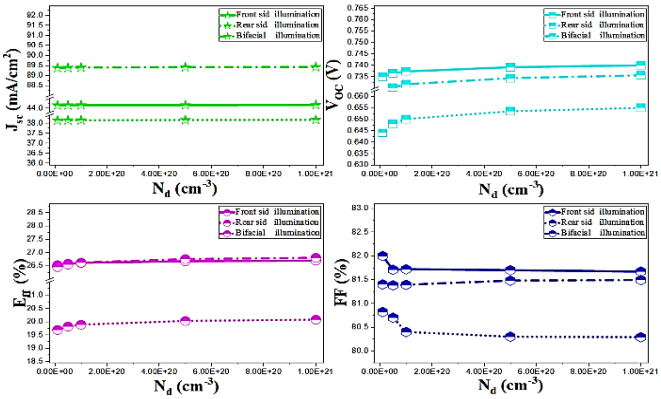


**Figure 3**. Variation of Jsc, Voc, FF, and $E_{ff}$with Doping Concentration in the n-a-Si:H Layer under Front and Rear Illumination

**Table 5. Front–Rear Performance Differences ($\Delta J_{SC}$, $\Delta V_{OC}$, $\Delta E_{ff}$, $\Delta FF$) and Front–to-Rear Ratio at Selected Doping concentration**

| ***Doping concetratio*** $(cm^{-3})$ | $\Delta J_{SC}(m/cm^2)$ | $\Delta V_{OC}$(V) | $\Delta E_{ff}$( %) | $\Delta FF$ | $Rear-to-front\ Ratio$(%) |
|---|---|---|---|---|---|
| $1.10^{19}$ | 6.012 | 0.091 | 6.834 | 1.56 | 74.23 |
| $1.10^{20}$ | 6.012 | 0.0871 | 6.723 | 1.55 | 74.73 |
| $5.10^{20}$ | 6.003 | 0.0856 | 6.644 | 1.4 | 75.09 |

## 4.3. Effect of n-a-Si:H layer Thickness on HJ Silicon Solar Cells under Front and Rear Illumination

Finally, the effect of the n-a-Si:H emitter-layer thickness on the photovoltaic performance of the HJ silicon solar cell was investigated. The emitter thickness was varied systematically over the range of [5–10] nm under asymmetric front-side and rear-side illumination conditions. All other structural and physical parameters were kept constant to isolate the effect of emitter thickness. To isolate the effect of the emitter thickness, a fixed interface-trap density of $10^{10}\ cm^{-2}$ was assumed at the front interface, while a rear interface-trap density of $10^{9}\ cm^{-2}$.was used at the rear interface. The simulations were performed at 300 K under the standard AM1.5G solar spectrum. The calculated photovoltaic parameters are presented in *figure 4. (a)–(d)*. The results show that, $J_{SC}^{Front}$, $J_{SC}^{Rear}$, $J_{SC}^{Bifacial}$ *and* $V_{OC}^{Front}$, $V_{OC}^{Rear}$, $V_{OC}^{Bifacial}$ *and* $E_{ff}^{Front}$, $E_{ff}^{Rear}$, $E_{ff}^{Bifacial}$ ,$FF^{Front}$,$FF^{Rear}$, $FF^{Bifacial}$ the photovoltaic parameters exhibit a slight decrease with increasing thickness of the n-a-Si:H emitter layer. This behavior may be attributed to the longer transport path that hoto-generated carriers need to traverse before reaching the relevant hetero-interface and electrical contact. Increasing the emitter thickness may therefore increase transport and recombination losses and contribute to an increase in the effective series resistance, consequently reducing the photovoltaic performance. Conversely, a thinner emitter layer may facilitate carrier extraction by reducing the transport path and the associated losses. Therefore, the 5 nm thickness should be interpreted as the best-performing thickness within the investigated range rather than as evidence of a global optimum. This behavior is consistent with previous findings reported in the literature [23],[27],[28].

Interestingly, the rear-to-front efficiency ratio: $\text{Ratio}(\text{E}_{ff}) = \frac{\text{E}_{ff}^{Rear}}{\text{E}_{ff}^{Front}}$ exhibits an increasing trend, rising from 73.63% to 74.23% as the thickness of the n-a-Si emitter layer increases. This indicates that the rear-side efficiency becomes relatively closer to the front-side efficiency at higher emitter thicknesses.

The observed variation in the front–rear efficiency asymmetry reflects the different sensitivities of the front- and rear-illumination configurations to changes in emitter thickness. This is also evident from the results presented in *table 6*, where the difference between the front- and rear-side

FOREX Publication
Open Access | Rapid and quality publishing
International Journal of Electrical and Electronics Research (IJEER)
Research Article | Volume 14, Issue 3 | Pages 759-770| e-ISSN: 2347-470X

photovoltaic parameters decreases as the n-a-Si:H emitter-layer thickness increases.↑ $\Delta J_{SC} = J_{SC}^{Front} - J_{SC}^{Rear}$ , ↑ $\Delta V_{OC} = V_{OC}^{Front} - V_{OC}^{Rear}$ , ↑ $\Delta E_{ff} = E_{ff}^{Front} - E_{ff}^{Rear}$ , ↑ $\Delta FF = FF^{Front} - FF^{Rear}$ , Overall, the results indicate that a thinner n-a-Si:H emitter layer is favorable for photovoltaic performance within the investigated range. The variation in the front–rear differences further indicate that the two illumination configurations respond differently to changes in emitter thickness. A wider thickness range would be required to determine whether a better-performing thickness exists outside the investigated range.

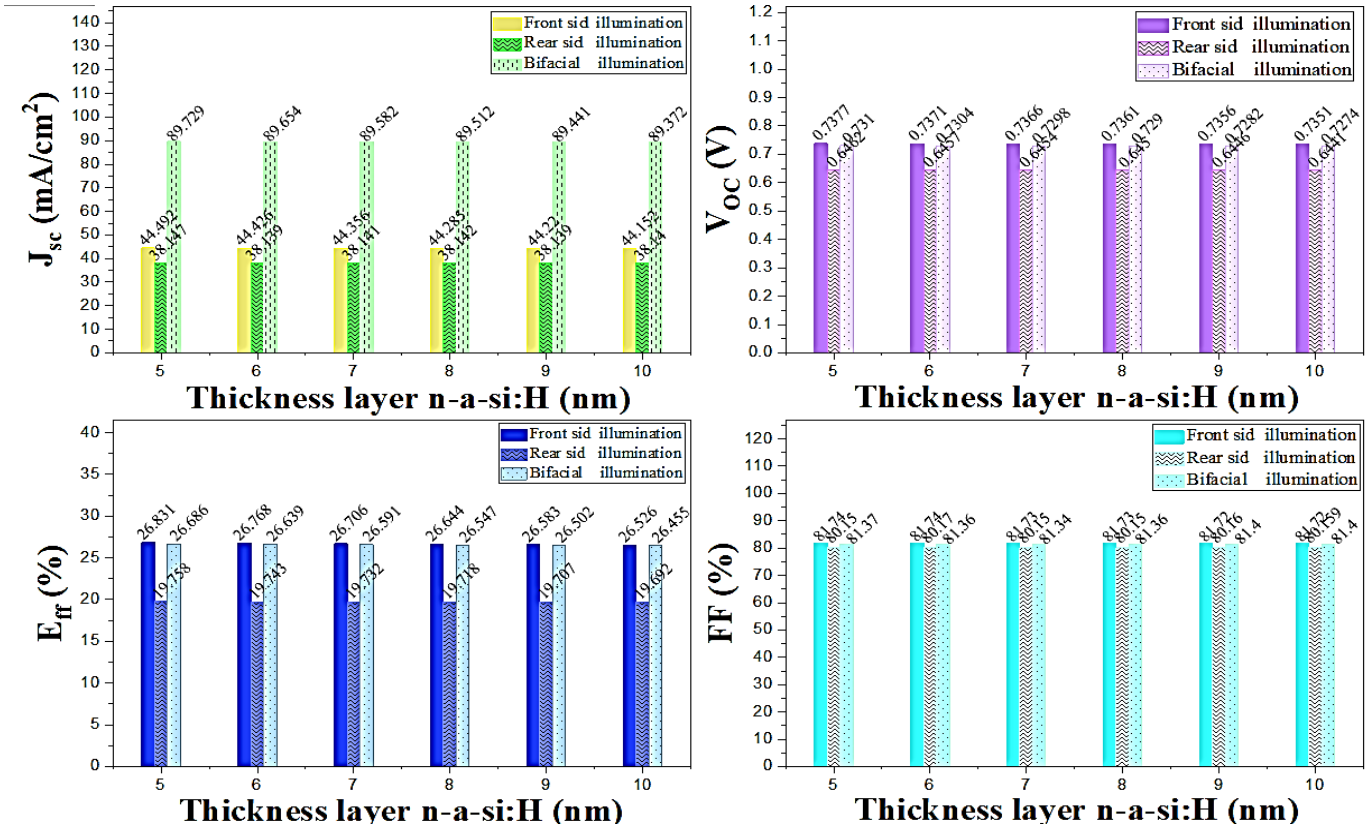


**Figure 4.** Variation of Jsc, Voc, FF, and $E_{ff}$ with thickness in the n-a-Si:H Layer under Front and Rear Illumination

**Table 6. Front–Rear Performance Differences ($\Delta J_{SC}$, $\Delta V_{OC}$, $\Delta E_{ff}$, $\Delta FF$) and Front–to-Rear Ratio at Selected thickness layer**

| $Thickness\ layer(nm)$ | $\Delta J_{SC}(mA/cm^2)$ | $\Delta V_{OC}$(V) | $\Delta E_{ff}$(%) | $\Delta FF$ (%) | $Rear-to-front\ Ratio$(%) |
|---|---|---|---|---|---|
| **5** | 6.345 | 0.0915 | 7.073 | 1.59 | 73.63 |
| **7** | 6.215 | 0.0912 | 6.974 | 1.58 | 73.88 |
| **10** | 6.012 | 0.091 | 6.834 | 1.56 | 74.23 |

## 4.4. SRH Recombination Analysis of the Bifacial Solar Cell

To further elucidate the physical origin of the electrical behavior associated with the most interface- trap-sensitive n-a-Si:H/c-Si interface, the spatial distribution of the volumetric Shockley–Read–Hall (SRH) recombination rate was analyzed within the c-Si absorber, as shown in *figure 5*. The SRH recombination rate is described by the Shockley–Read–Hall model as [29],

$$R_{SRH} = \frac{np - n_i^2}{\tau_p(n+n_1) + \tau_n(p+p_1)} \quad (13)$$

Where $n_1 = n_i . exp[(E_T - E_i)/k_B T]$

$p_1 = n_i . exp[(E_i - E_T)/k_B T]$

where $n$ and $p$ are the electron and hole concentrations, $n_i$ is the intrinsic carrier concentration, $\tau_n$ and $\tau_p$ are the carrier lifetimes, and $n_1$ and $p_1$ are the trap-related carrier concentrations and $E_T$ is the trap energy level, $k_B$ is the Boltzmann constant, and $E_i$ is the intrinsic Fermi level. *Figure 5* presents the spatial distribution of the volumetric SRH recombination rate as a function of the x-coordinate within the c-Si absorber for asymmetric interface-trap conditions, with $10^{10}\ cm^{-2}$ at the front n-a-Si:H/c-Si interface and $10^{9}\ cm^{-2}$

FOREX Publication
Open Access | Rapid and quality publishing
International Journal of Electrical and Electronics Research (IJEER)
Research Article | Volume 14, Issue 3 | Pages 759-770| e-ISSN: 2347-470X

at the rear c-Si/p-a-Si:H interface. The profile illustrates how the asymmetric interface conditions influence the spatial distribution of carrier recombination within the c-Si layer. The non-uniform distribution of the SRH recombination rate indicates that recombination is spatially dependent within the absorber rather than being uniformly distributed across the c-Si layer. This behavior may be associated with the influence of the interface conditions on the carrier concentrations and carrier transport near the front and rear surfaces, which consequently affects the local SRH recombination rate inside the absorber. Therefore, the SRH recombination profile provides a physical link between the interface-defect conditions and the resulting electrical behavior of the bifacial device. In particular, it helps explain how the asymmetric defect conditions at the two interfaces can modify the recombination distribution within the c-Si absorber and contribute to the observed front–rear performance asymmetry.

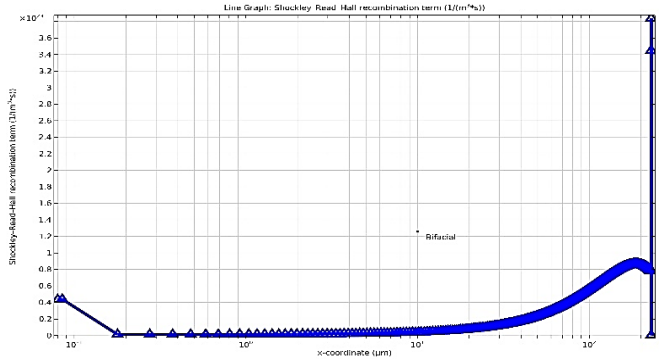


**Figure 5.** Spatial distribution of the volumetric SRH recombination rate within the c-Si absorber under asymmetric interface-trap conditions

## 5. VALIDATION OF COMSOL-SIMULATION J-V CHARACTERISTICS AND EFFICIENCY RATIO AGAINST NUMERICAL LITERATURE

This section assesses the reliability of the COMSOL Multiphysics model through comparison of the simulated photovoltaic parameters with experimentally reported data from the literature. The simulated current density–voltage (J–V) characteristics under front and rear illumination conditions are shown in *figure 6.*

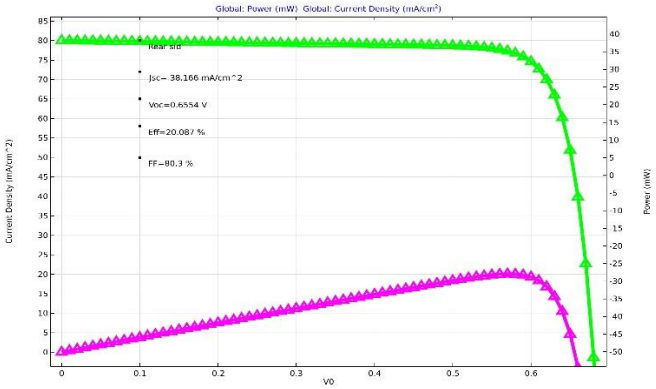


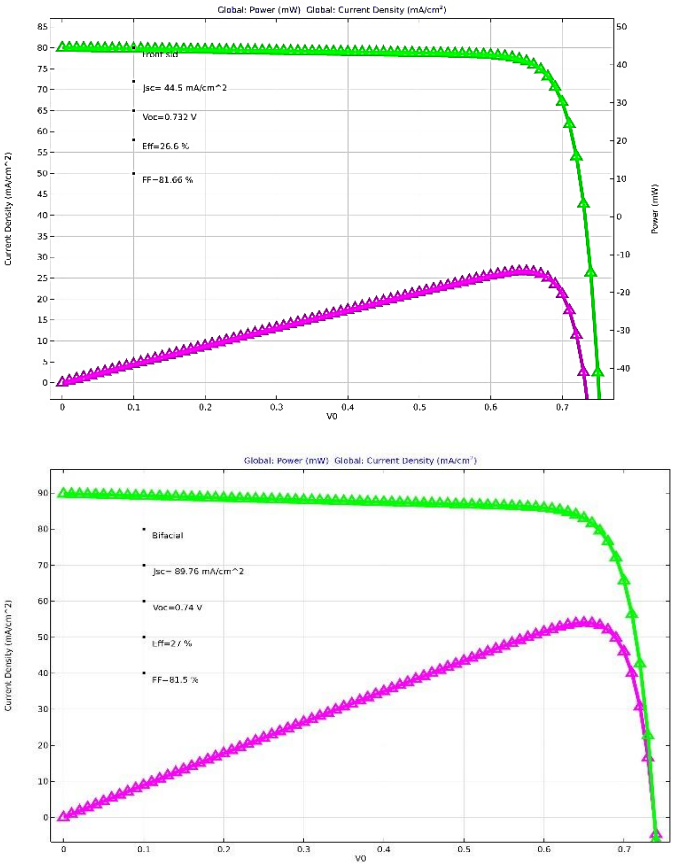


**Figure 6.** Comparison of the photovoltaic parameters (Jsc, Voc, FF, and $E_{ff}$) under front- and rear-side illumination for the silicon heterojunction (HJ) solar cell

The fill factor $FF$, photovoltaic conversion efficiency $E_{ff}$, short-circuit current density $J_{SC}$, and open-circuit voltage $V_{OC}$ are key performance parameters used to evaluate solar cell behavior. The photovoltaic of current density ratio is defined and calculated using the following expression:

$$\text{Ratio}(\text{J}_{SC}) = \frac{\text{J}_{SC}^{Rear\ illumunation}}{\text{J}_{SC}^{Front\ illumunation}} \quad (14)$$

The photovoltaic of open circuit voltage ratio is defined and calculated using the following expression:

$$\text{Ratio}(\text{V}_{OC}) = \frac{\text{V}_{OC}^{Rear\ illumunation}}{\text{V}_{OC}^{Front\ illumunation}} \quad (15)$$

The photovoltaic of conversion efficiency ratio is defined and calculated using the following expression

$$\text{Ratio}(\text{E}_{ff}) = \frac{\text{E}_{ff}^{Rear\ illumunation}}{\text{E}_{ff}^{Front\ illumunation}} \quad (16)$$

The photovoltaic of fill factor ratio is defined and calculated using the following expression:

$$\text{Ratio}(\text{FF}) = \frac{FF^{Rear\ illumination}}{FF^{Front\ illumination}} \quad (17)$$

The simulated photovoltaic performance was compared with the experimental results reported for industrialized bifacial

FOREX Publication
Open Access | Rapid and quality publishing
International Journal of Electrical and Electronics Research (IJEER)
Research Article | Volume 14, Issue 3 | Pages 759-770| e-ISSN: 2347-470X

silicon solar cells fabricated on large-area CZ monocrystalline silicon wafers. The reference cells employed industrially relevant processing techniques, including $BBr_3$ and $POCl_3$ diffusions, PECVD $SiN_x$ deposition, and screen-printed contacts. The reported front- and rear-side efficiencies were 16.6% and 12.8%, respectively, corresponding to a rear-to-front efficiency ratio of approximately 77.1%, derived from these reported values. For the present simulated cell, the corresponding rear-to-front efficiency ratio is 75.5%, which is close to the approximately 77.1% ratio derived from the experimental results reported by Yang et al. [30], for an additional experimental comparison, Ref. [31] reported front- and rear-side efficiencies of 20.05% and 19.07%, respectively, corresponding to a rear-to-front efficiency ratio of approximately 95.1%.as shown in *figure 7*. This comparison provides an independent benchmark for assessing the front–rear performance asymmetry of the present model. However, the reference devices differ from the present structure in terms of cell architecture, contact materials, fabrication technology, and modeling assumptions. Therefore, these comparisons are regarded as literature-based numerical benchmarks rather than as direct experimental validation of the complete simulated device.

**Table.7 Photovoltaic performance parameters under front, rear, and bifacial illumination**

| Illumination condition | $J_{SC}$ $(mA/cm^2)$ | $V_{OC}$ $(V)$ | $E_{ff}$ (%) | $FF$(%) |
|---|---|---|---|---|
| Bifacial | 89.76 | 0.74 | 27.00 | 81.50 |
| Front Sid | 44.50 | 0.73 | 26.60 | 81.66 |
| Rear Sid | 38.16 | 0.65 | 20.09 | 80.30 |
| Rear − to − front Performar ratio (%) | 85.76 | 89.53 | 75.51 | 98.33 |
| Front Sid Ref [30] | 34.90 | 0.62 | 16.60 | 77.20 |
| Rear Sid Ref [30] | 26.80 | 0.61 | 12.80 | 78.20 |
| Front Sid Ref [31] | 38.17 | 0.655 | 20.05 | 78.83 |
| Rear Sid Ref [31] | 36.16 | 0.651 | 19.07 | 79.49 |

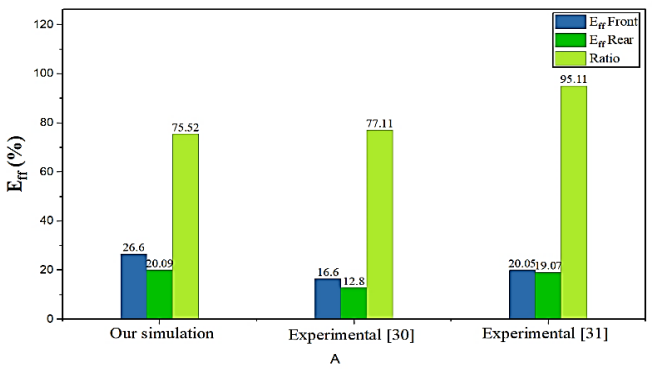


**Figure 7**. Bifacial HJ Ratio: Comparison with References

The simulated, $J_{SC}, V_{OC}, FF\ and\ E_{ff}$ values were compared with the experimental results reported in Refs. [30] and [31], as summarized in *table 7*. To quantitatively assess the differences between the present model and the experimental reference, the absolute deviation $\Delta X_{abs}$ and relative deviation $\delta X$ were calculated using:

$$\Delta X_{abs} = |X_{Sim} - X_{ref}| \quad (18)$$

$$\delta X = \frac{|X_{Sim} - X_{ref}|}{X_{ref}} \times 100 \quad (19)$$

Where $(X)$ represents $J_{SC}, V_{OC}, FF\ and\ E_{ff}$ and the subscripts "sim" and "ref" denote the simulated and reference values, respectively. For front-side illumination, the relative deviations in $J_{SC}, V_{OC}, FF\ and\ E_{ff}$ with respect to Ref. [30] are $27.51\%, 18.06\%, 5.78\%,$ and $60.24\%$, respectively, corresponding to absolute deviations of $9.60\ mA/cm^2, 0.112\ V,$ 4.4percentage points, and 10.00 percentage points For rear-side illumination, the corresponding relative deviations are $42.39\ \%, 6.56\ \%, 2.69\%, and\ 56.95\%$, with absolute deviations of $11.36\ mA/cm^2$, $0.04\ V,$ 2.10 percentage points , $and$ 7.29 percentage points respectively.

The observed differences between the simulated and experimental photovoltaic parameters can be primarily attributed to differences in device architecture, material configuration, and modeling assumptions. The present model considers an asymmetric bifacial HIT solar cell with distinct front and rear carrier-selective layers and contact configurations, whereas the experimental bifacial crystalline-silicon solar cells reported in Refs. [30] and [31] have different device structures and material configurations. Consequently, the compared devices may exhibit different optical absorption, carrier transport, recombination, contact, and interface characteristics under front- and rear-side illumination. In the present model, the use of n-a-Si and p-a-Si carrier-selective layers, ITO-based contacts, and distinct front and rear interfaces results in different carrier-collection and recombination conditions on the two sides of the device. These structural asymmetries are particularly relevant to the rear-side photovoltaic response and can contribute to the observed differences from the experimental references. Therefore, the comparisons with Refs. [30] and [31] should be regarded as independent experimental benchmarks for quantitatively assessing the present model rather than as direct validation against identical device structures.

For front-side illumination, the absolute deviations in $J_{SC}, V_{OC}, FF\ and\ E_{ff}$ are 6.33 mA/cm², 0.075 V, 2.83 percentage points, and 6.55 percentage points, corresponding to relative deviations of 16.58%, 11.45%, 3.59%, and 32.67%, respectively. For rear-side illumination, the corresponding absolute deviations are 2.00 mA/cm², 0.001 V, 0.81 percentage points, and 1.02 percentage points, with relative deviations of 5.53%, 0.15%, 1.02%, and 5.35%, respectively. The relatively small deviations observed for the rear-side $J_{SC}, V_{OC}, FF\ and\ E_{ff}$ indicate a closer agreement between the present simulations and the experimental results reported in Ref. [31], particularly under rear-side illumination. Overall,

FOREX Publication
Open Access | Rapid and quality publishing
International Journal of Electrical and Electronics Research (IJEER)
Research Article | Volume 14, Issue 3 | Pages 759-770| e-ISSN: 2347-470X

the comparisons with Refs. [30] and [31] provide independent experimental benchmarks for quantitatively assessing the simulated photovoltaic parameters. The differences observed between the simulated and experimental results are consistent with variations in device structure, material properties, contact configuration, and modeling assumptions, and therefore the comparisons support the quantitative assessment of the present model without implying complete experimental validation of an identical device.

## 5. CONCLUSIONS

This work presented a numerical investigation of a bifacial silicon heterojunction (HJ) solar cell based on the IMAI/n-a-Si:H/c-Si/p-a-Si:H/ITO structure using COMSOL Multiphysics. The device was analyzed under front-side, rear-side, and simultaneous bifacial illumination conditions, with particular emphasis on the effects of interface-trap density, donor concentration in the n-type amorphous silicon layer, and emitter thickness. The results demonstrate that the photovoltaic performance is strongly governed by interface recombination asymmetry and emitter design. In particular, the asymmetric interface-trap configuration, with $10^{10}$ $cm^{-2}$ at the n-a-Si:H/c-Si front interface and $10^{9}$ $cm^{-2}$ at the c-Si/n-a-Si:H rear interface leads to a pronounced front–rear asymmetry in carrier collection and photovoltaic performance. The parametric variations of donor concentration $5 \times 10^{20}$ $cm^{-3}$ and emitter thickness 5 nm indicate that the selected parameter values can influence the electrical characteristics of the device by affecting carrier transport and collection. Based on the investigated parameter ranges, the selected parameter set yields simulated conversion efficiencies of 26.6% under front-side illumination, 20.09% under rear-side illumination, and 27% under simultaneous bifacial illumination. The corresponding rear-to-front efficiency ratio is 75.5%, indicating that the rear-side photovoltaic response remains lower than the front-side response. The spatial analysis of the volumetric Shockley–Read–Hall recombination rate within the c-Si absorber further demonstrates the non-uniform nature of carrier recombination under asymmetric interface conditions. This provides a physical interpretation of the front–rear performance asymmetry and highlights the role of interface conditions in determining the carrier transport and recombination behavior of the bifacial device.

Overall, the results highlight the importance of precise interface engineering and appropriate selection of emitter properties for controlling recombination losses and improving the performance balance of bifacial heterojunction silicon solar cells. The comparison with previously reported numerical and experimental results provides an independent benchmark for the present simulations and supports the physical consistency of the developed numerical framework, while the remaining differences can be attributed to variations in device architecture, material parameters, interface properties, and modeling assumptions. Since the investigated parameters were varied using a one-factor-at-a-time (OFAT) approach, the present study evaluates individual parameter sensitivities and does not account for parameter interactions or establish a global multi-parameter optimum.

**Acknowledgments:** I also extend my deep thanks to the Materials Laboratory for Renewable Energy Applications and Valorization (LMAVER), University of Laghouat, Algeria, and the Laboratory of Applied Sciences and Didactics, Higher Normal School of Laghouat, Algeria, for their scientific support and the research environment they provided.

## REFERENCES

[1] Barbir, F.; Veziroğlu, T.N.; Plass, H.J., Jr. Environmental damage due to fossil fuels use. Int. J. Hydrogen Energy 1990, 15, 739–749.

[2] Muñoz, D.; Desrues, T.; Ribeyron, P.-J. a-Si/c-Si heterojunction solar cells: A smart choice for high efficiency solar cells. In Physics and Technology of Amorphous/Heterostructure Silicon Solar Cells: Engineering Materials; 2012; pp. 539–572. https://doi.org/10.1007/978-3-642-22275-7.

[3] Korte, L.; Conrad, E.; Angermann, H.; Stangl, R.; Schmidt, M. Advances in a-Si/c-Si heterojunction solar cell fabrication and characterization. Sol. Energy Mater. Sol. Cells 2009, 93, 905–910.

[4] Wolf, S.D.; Descoeudres, A.; Holman, Z.C.; Ballif, C. High efficiency silicon heterojunction solar cells: A review. Green 2012, 12, 7–24.

[5] Shafiee, S.; Topal, E. When will fossil fuel reserves be diminished? Energy Policy 2009, 37, 181–189. https://doi.org/10.1016/j.enpol.2008.08.016.

[6] Elza, V.B.; Babu, V.S.; Abraham, N. Materials today: Proceedings perspective on machine learning based investigated materials to realize stable-efficient-toxin free (S-E-T) perovskite solar cells. Mater. Today Proc. 2023. https://doi.org/10.1016/j.matpr.2023.04.640.

[7] Verma, A.; Pethe, A. Modelling and analysis of multi-junction photovoltaic cells. In Proceedings of the 2020 IEEE 17th India Council International Conference (INDICON), December 2020; pp. 1–6.

[8] Jost, M.; Kegelmann, L.; Korte, L.; Albrecht, S. Monolithic perovskite tandem solar cells: A review of the present status and advanced characterization methods toward 30% efficiency. Adv. Energy Mater. 2020. https://doi.org/10.1002/aenm.201904102.

[9] Ghozati, S.B.; Ebong, A.U.; Honsberg, C.B.; Wenham, S.R. Improved fill-factor for the double-sided buried-contact bifacial silicon solar cell. Sol. Energy Mater. Sol. Cells 1998, 51, 121–128.

[10] Cuevas, A.; Luque, A.; Eguren, J.; Del Alamo, J. High efficiency bifacial back surface field solar cells. Sol. Cells 1981, 3, 337–340.

[11] Del Canizo, C.; Moehlecke, A.; Zanesco, I.; Tobias, I.; Luque, A. Analysis of a technology for CZ bifacial solar cells. IEEE Trans. Electron Devices 2001, 48, 2337–2341.

[12] Duran, C. Bifacial Solar Cells: High Efficiency Design, Characterization, Modules Applications; 2012; p. 130.

[13] Rauer, M.; et al. Monofacial IV measurements of bifacial silicon solar cells in an inter-laboratory comparison. In Proceedings of the 32nd European Photovoltaic Solar Energy Conference and Exhibition (EU PVSEC), 2016; pp. 915–921. https://doi.org/10.4229/eupvsec20162016-2bv.7.25.

[14] Moehlecke, A.; da C. Osório, V.; Zanesco, I.; Osório, C.; Zanesco, I. Analysis of thin bifacial silicon solar cells with locally diffused and selective back surface field. Mater. Res. 2014, 17, 1328–1335.

[15] COMSOL Multiphysics. COMSOL Multiphysics Reference Manual; COMSOL: Grenoble, France, 2013.

[16] Burgelman, M.; Decock, K.; Niemegeers, A.; Verschraegen, J.; Degrave, S. SCAPS Manual; University of Ghent: Ghent, Belgium, 2016.

[17] COMSOL Multiphysics. Introduction to COMSOL Multiphysics®; COMSOL Multiphysics: Burlington, MA, USA, 1998.

[18] Froitzheim, A.; Stangl, R.; Elstner, L.; Kriegel, M.; Fuhs, W. AFORS-HET: A computer-program for the simulation of heterojunction solar cells to be distributed for public use. In Proceedings of the 3rd World

International Journal of
Electrical and Electronics Research (IJEER)
Research Article | Volume 14, Issue 3 | Pages 759-770| e-ISSN: 2347-470X

Conference on Photovoltaic Energy Conversion, 2003; Volume 1, pp. 279–282.

[19] Polyanskiy, M.N. Refractiveindex.info database of optical constants. Sci. Data 2024, 11, 94. https://doi.org/10.1038/s41597-023-02898-2.

[20] Shockley, W.; Read, W.T., Jr. Statistics of the recombinations of holes and electrons. Phys. Rev. 1952, 87, 835. https://doi.org/10.1103/PhysRev.87.835.

[21] Green, M.A. Silicon Solar Cells: Advanced Principles & Practice; UNSW Press: Sydney, Australia, 1995.

[22] Hacini, A.; Ali, A.H.; Harkat, L.; Nayan, N.; Adnan, N.N.; Azali, M.M.; Sani, N. Effect of laser fluence on the ITO/Mo-Ag/ITO multilayer thin film for a-Si (n)/c-Si (p)/a-Si (p)/Al heterojunction solar cells. Sol. Energy 2024, 284, 113042. https://doi.org/10.1016/j.solener.2023.113042.

[23] Lisheng, W.; Fengxiang, C.; Yu, A. Simulation of high efficiency heterojunction solar cells with AFORS-HET. J. Phys. Conf. Ser. 2011, 276, 012177.

[24] Wang, F.; Gao, Y.; Pang, Z.; Yang, L.; Yang, J. Insights into the role of the interface defects density and the bandgap of the back surface field for efficient p-type silicon heterojunction solar cells. RSC Adv. 2017, 7, 26776–26782.

[25] Hashemi, M.; Minbashi, M.; Ghorashi, S.M.B.; Ghobadi, A. A modeling study on utilizing low temperature sprayed In2S3 as the buffer layer of CuBaSn(S,Se) solar cells. Sci. Rep. 2021, 11, 20038.

[26] Shu, Z.; Das, U.; Allen, J.; Birkmire, R.; Hegedus, S. Experimental and simulated analysis of front versus all-back-contact silicon heterojunction solar cells: Effect of interface and doped a-Si layer defects. Prog. Photovolt.: Res. Appl. 2015, 23, 78–93.

[27] Revollo, H.; Ferrada, P.; Martin, P.; Marzo, A.; Del Campo, V. HIT solar cell modeling using graphene as a transparent conductive layer considering the Atacama Desert solar spectrum. Appl. Sci. 2023, 13, 9323.

[28] Benchiheb, A.; Benchiheb, N.; Saidi, Y.; Dib, S. Effects of doping profile and temperature on the bifacial solar cell performances. In Proceedings of the 2022 19th International Multi-Conference on Systems, Signals & Devices (SSD), May 2022; pp. 425–428.

[29] Sze, S.M. Physics of Semiconductor Devices, 2nd ed.; John Wiley & Sons: New York, NY, USA, 1981.

[30] Yang, L.; Ye, Q.H.; Ebong, A.; Song, W.T.; Zhang, G.J.; Wang, J.X.; Ma, Y. High efficiency screen printed bifacial solar cells on monocrystalline CZ silicon. Prog. Photovolt.: Res. Appl. 2011, 19, 275–279.

[31] Gonsui, S.; Goda, S.; Sugibuchi, K.; Ishikawa, N.; Honda, K.; Zama, H. N-type high efficiency bifacial silicon solar cell with the extremely high bifaciality of 96% in average fabricated by using conventional diffusion method. In Proceedings of the 28th European Photovoltaic Solar Energy Conference and Exhibition (EU PVSEC), Paris, France, 2013.

© 2026 by the Wafa Bakhat, Asma Benchiheb, and Hamza Lidjici, Fatima Zahra Bakhat. Submitted for possible open access publication under the terms and conditions of the Creative Commons Attribution (CC BY) license (http://creativecommons.org/licenses/by/4).